



HAL
open science

Highly spatially resolved mapping of the piezoelectric potentials in InGaN quantum well structures by off-axis electron holography

V. Boureau, D. Cooper

► **To cite this version:**

V. Boureau, D. Cooper. Highly spatially resolved mapping of the piezoelectric potentials in InGaN quantum well structures by off-axis electron holography. *Journal of Applied Physics*, 2020, 128 (15), 10.1063/5.0020717 . cea-04938462

HAL Id: cea-04938462

<https://cea.hal.science/cea-04938462v1>

Submitted on 10 Feb 2025

HAL is a multi-disciplinary open access archive for the deposit and dissemination of scientific research documents, whether they are published or not. The documents may come from teaching and research institutions in France or abroad, or from public or private research centers.

L'archive ouverte pluridisciplinaire **HAL**, est destinée au dépôt et à la diffusion de documents scientifiques de niveau recherche, publiés ou non, émanant des établissements d'enseignement et de recherche français ou étrangers, des laboratoires publics ou privés.

RESEARCH ARTICLE | OCTOBER 20 2020

Highly spatially resolved mapping of the piezoelectric potentials in InGaN quantum well structures by off-axis electron holography

V. Boureau ; D. Cooper  



J. Appl. Phys. 128, 155704 (2020)

<https://doi.org/10.1063/5.0020717>



Articles You May Be Interested In

Mapping of the electrostatic potentials in MOCVD and hybrid GaN tunnel junctions for InGaN/GaN blue emitting light emitting diodes by off-axis electron holography correlated with structural, chemical, and optoelectronic characterization

J. Appl. Phys. (July 2021)

Three-dimensional measurement of Mg dopant distribution and electrical activity in GaN by correlative atom probe tomography and off-axis electron holography

J. Appl. Phys. (February 2020)

The underlying micro-mechanism of performance enhancement of non-polar *n*-ZnO/*p*-AlGaIn ultraviolet light emitting diode with *i*-ZnO inserted layer

Appl. Phys. Lett. (January 2018)



Journal of Applied Physics

Special Topics Open for Submissions

[Learn More](#)

Highly spatially resolved mapping of the piezoelectric potentials in InGaN quantum well structures by off-axis electron holography

Cite as: J. Appl. Phys. 128, 155704 (2020); doi: 10.1063/5.0020717

Submitted: 3 July 2020 · Accepted: 27 September 2020 ·

Published Online: 20 October 2020



View Online



Export Citation



CrossMark

V. Boureau^{1,2}  and D. Cooper^{1,a)} 

AFFILIATIONS

¹Univ. Grenoble Alpes, CEA, LETI, F-38000 Grenoble, France

²Interdisciplinary Center for Electron Microscopy (CIME), EPFL, CH-1015 Lausanne, Switzerland

^{a)}Author to whom correspondence should be addressed: david.cooper@cea.fr

ABSTRACT

The internal fields in 2.2 nm thick InGaN quantum wells in a GaN LED structure have been investigated by using aberration-corrected off-axis electron holography with a spatial resolution of better than 1 nm. To improve the spatial resolution, different types of off-axis electron holography acquisitions have been used, including pi phase shifting and phase shifting holography. A series of electron holograms have been summed up to simultaneously improve the sensitivity in the measurements. A value of 20% of indium concentration in the quantum wells has been obtained by comparing the deformation measured by dark-field electron holography and geometrical phase analysis to finite element simulations. The electrostatic potential has then been measured by off-axis electron holography. The mean inner potential difference between the InGaN quantum wells and the GaN quantum barriers is high compared to the piezoelectric potential. Due to the improved spatial resolution, it is possible to compare the experimental results to simulations and remove the mean inner potential component to provide a quantitative measurement of the piezoelectric potential.

Published under license by AIP Publishing. <https://doi.org/10.1063/5.0020717>

INTRODUCTION

There is a need to measure the electric fields and potentials at high-resolution in semiconductor materials in order to relate their electrical and optical properties to their structure. An important example is the InGaN quantum well (QW) structure, which is used in light emitting diodes.^{1,2} One of the major factors that limit the light output is the presence of polarization fields that originate from the wurtzite crystal structure. Along with the spontaneous polarization, there is a strong piezoelectric polarization that originates from mechanical strain in the epitaxially grown quantum wells leading to surface charges at the interfaces.³ In the InGaN/GaN system, the spontaneous and piezoelectric polarization act in opposite directions, which further complicates the understanding.⁴ These piezoelectric fields can be high enough to localize carriers at the interfaces and create energy barriers that hinder carrier transport.⁵ As such, research is needed in order to understand how to lower the piezoelectric polarization using novel substrates^{6–8} or by integrating the diodes into 3D device structures.⁹ In order to assess if these methods are indeed reducing the piezoelectric fields,

characterization methods with the appropriate sensitivity and spatial resolution are required. In this paper, we show that off-axis electron holography can be used to measure the piezoelectric fields in a multiple InGaN quantum wells structure. A test specimen nominally containing six 2.5 nm wide InGaN QWs each separated by 13 nm wide quantum barriers (QBs) on a GaN substrate grown by molecular beam epitaxy (MBE) along the c-plane (0001) direction has been studied. The In content has been obtained from measurements of the deformation obtained by dark-field electron holography (DFEH) and geometric phase analysis (GPA). Then, simulations of the expected electrostatic potentials for the obtained In concentration in the specimen have been performed such that the accuracy of the measurements of the electrostatic potentials can be assessed. For such small structures, the spatial resolution becomes important and three different reconstruction methods have been used. Standard off-axis electron holography has been compared to pi phase shifting and phase shifting holography. Typically, when electron holograms are acquired for optimized spatial resolution, this is at the expense of sensitivity. In this work, stacks of electron holograms have been

10 February 2025 13:43:53

acquired, such that the sensitivity is simultaneously improved with the spatial resolution.

OFF-AXIS ELECTRON HOLOGRAPHY METHODS

Off-axis electron holography (from now referred to as electron holography) is a transmission electron microscopy (TEM) based technique that uses an electron biprism to interfere a coherent electron wave that has passed through a region of interest with a wave that has passed through only vacuum. From the resulting interference pattern, known as an electron hologram, the phase and the amplitude of the electron wave can be reconstructed using a simple Fourier reconstruction procedure.¹⁰ Equation (1) shows that in the absence of a magnetic field, the phase, $\phi(\mathbf{r})$, of an electron traveling along the z direction is sensitive to the electrostatic potential, $V(\mathbf{r})$,

$$\phi(\mathbf{r}) = \frac{e}{\hbar v} \int_{-\infty}^{+\infty} V(\mathbf{r}) dz, \quad (1)$$

where e is the electron charge, v is the electron velocity, and \hbar is the reduced Planck's constant.¹¹ This formula is valid under the weak phase object approximation, which assumes that the specimen does not change the electron beam amplitude. This approximation fails for thicker specimens when multiple scattering processes occur. Thus, it is necessary to carefully tilt the specimen to a weakly diffracting condition. This reduces the effect of dynamical diffraction, which modifies the phase strongly and leads to uninterpretable results. Then, the change in phase is directly proportional to the sum of the different contributions of the electrostatic potentials. For semiconductor specimens, this is the sum of the mean inner potential (MIP) of the material (V_{MIP}) plus variations of the electrostatic potential arising from the presence of active dopants (V_{dopants}) and piezoelectric fields (V_{piezo}).^{12,13} The measured change in phase relative to a reference is then given by

$$\phi = C_E \int_0^t (V_{\text{MIP}} + V_{\text{dopants}} + V_{\text{piezo}}) dz, \quad (2)$$

where t is the thickness of the specimen and $C_E = \frac{e}{\hbar v}$ is a constant equal to $0.0065 \text{ rad nm}^{-1} \text{ V}^{-1}$ for 300 kV electrons.¹³ Today, there are many studies that can be found in the literature where electron holography has been used to measure the dopant potentials in nitride materials^{14–17} as well as the piezoelectric fields in both InGaN^{18–25} and AlGaN^{26–28} QW structures.

The deformation in the region of interest can be measured by dark-field electron holography.²⁹ Here, the specimen is intentionally tilted to a highly diffracting two-beam condition and an objective aperture is used to select a diffracted beam corresponding to the lattice planes of interest. After the dark phase reconstruction, the deformation can be obtained using this so-called geometric phase map, ϕ_g ,

$$\phi_g(\mathbf{r}) = -2\pi \mathbf{g} \cdot \mathbf{u}(\mathbf{r}), \quad (3)$$

where \mathbf{g} is the reciprocal lattice vector of the reference crystal and \mathbf{u} is the displacement vector from which the displacement field can

be calculated.³⁰ The deformation is then proportional to the derivative of ϕ_g ,

$$\nabla \phi_g(\mathbf{r}) = -2\pi(\mathbf{g}_{\text{obj}}(\mathbf{r}) - \mathbf{g}_{\text{ref}}), \quad (4)$$

where ∇ is the spatial gradient and \mathbf{g}_{obj} and \mathbf{g}_{ref} are the reciprocal lattice vectors of the region of interest and reference, respectively. Therefore, it is possible, using the appropriate experimental conditions, to measure both the electrostatic and deformation fields in the same semiconductor specimen by off-axis electron holography.

To measure the polarization fields at the interfaces of InGaN QWs in GaN LED structures which are typically less than 5 nm wide, very high spatial resolutions are required. For standard off-axis electron holography phase reconstructions, the spatial resolution of the phase images is related to the fringe spacing. Figure 1(a) shows a schematic of the experimental setup in the TEM. To achieve higher spatial resolutions, interference fringes with a higher carrier frequency, q_c , are required. This can be achieved by increasing the positive voltage on the electron biprism to deflect the object and reference waves to higher angles. This provides a wider interference pattern with finer fringes by pushing the virtual sources S_1 and S_2 further apart. Figure 1(b) shows an example of an electron hologram containing the InGaN QWs. Here, the conventional TEM intensity image can be observed with the interference fringes that contain information about the phase of the electrons superimposed. To reconstruct the electron hologram, a Fourier transform is applied and a sideband is selected. Then, by performing an inverse Fourier transform, a complex image is obtained from which the phase and amplitude information about the specimen can be recovered.^{11–13} Figure 1(c) shows the Fourier transform of the hologram in (b). The centerband contains information about the conventional intensity image and the sideband contains information about the position and magnitude of the interference fringes. Thus, to avoid artifacts from the intensity image (corresponding to the amplitude squared) during reconstruction, a mask with a radius of $q_c/3$ is used, which provides a spatial resolution of three times the fringe spacing. However, the limited coherence of the electron beam means that the contrast of the holograms will decrease when higher biprism voltages are applied. The signal-to-noise in a reconstructed phase image is related to both the number of counts in the electron hologram and the contrast of the fringes.³¹ Therefore, when high spatial resolutions are required, typically this is at the expense of the signal-to-noise ratio. For standard microscope Lorentz settings in a FEI Titan TEM using a commercially available biprism, a fringe spacing of the order of 2 nm with contrast levels of around 20% are reasonably easy to obtain. For fringe spacings of 1 nm or less, the hologram contrast drops to very low values of 10% or less, reducing the signal-to-noise ratio of the reconstructed phase images. Longer acquisitions can be used to compensate, but mechanical and electrical stabilities in the microscope as well as drift of the specimen lead to additional problems. Thus, for higher spatial resolutions, it is now common to acquire a stack of electron holograms and then average them,^{32–35} taking into account the drift of the biprism, the electron beam wavefront, and the specimen.³⁶

The pi phase shifting method can be used to increase the spatial resolution in the hologram reconstruction step. Here, pairs

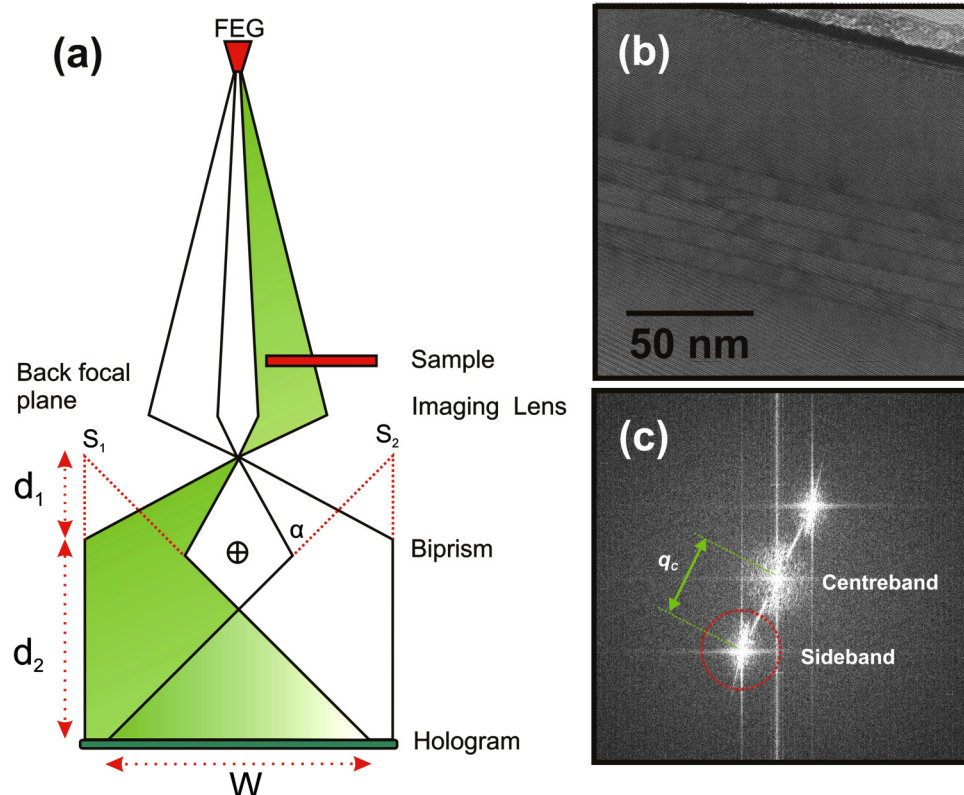


FIG. 1. (a) Schematic of off-axis electron holography. (b) An electron hologram of InGaN QWs in GaN. (c) Fourier transform of the hologram showing the centerband and sidebands.

of electron holograms are acquired, where the diffraction deflectors are used to shift the second hologram by π rad. Therefore, the subtraction of these two holograms from each pair suppresses the centerband and as such a mask of radius up to q_c can be used during the Fourier reconstruction, increasing the spatial resolution.³⁷ This approach has been fully automated in a FEI Titan TEM using the software Holoview. Large stacks of holograms with precise control of the hologram shift can be acquired to provide spatial resolutions of 1 nm with good signal-to-noise ratios.³⁵

Finally, the phase shifting method can also be used to recover the phase of the electrons in real space.³⁸ Here, the electron hologram is shifted such that several holograms are acquired in the $0-2\pi$ rad range. The phase can then be calculated for each pixel of the image from the local intensities of the hologram series.³⁹ The advantage of using this method is that the spatial resolution of the reconstructed phase is limited by the TEM optics, which in the case of an aberration-corrected FEI Titan operated in Lorentz mode is about 0.5 nm. Again, this has been automated by using the Holoview software that can precisely shift the hologram using the diffraction deflectors and acquire large stacks of phase shifted holograms to simultaneously obtain high signal-to-noise ratios and high spatial resolutions.

The fringe spacing of the holograms and the reconstruction methods are not the only constraints when trying to achieve high spatial resolutions. Due to the configuration of most TEMs, it is not possible to obtain an interference pattern with a field of view

larger than 30 nm when using the conventional objective lens. When performing experimental electron holography on semiconductors, a larger field of view is required. To achieve this, the objective lens is switched off and a Lorentz lens is used to form the image, which can provide fields of view in the 100 nm to micrometer range. However, the Lorentz lens has higher aberrations giving a spatial resolution of around 3 nm. The use of an image corrector can be used to reduce these aberrations and provide a spatial resolution of about 0.5 nm.

EXPERIMENTAL PROCEDURE

A TEM specimen was prepared using focused ion beam (FIB) milling in a FEI Strata 400 dual beam tool. The lift out was performed at 30 kV and a thin electron transparent window was prepared using an operating voltage of 16 kV before a cleaning step at 2 kV. To provide a vacuum reference region close to the region of interest, the specimen was covered with a $2\mu\text{m}$ thick layer of permanent ink before deposition of the tungsten protective layer, which was then removed during plasma cleaning. All of the TEM experiments were performed using a double aberration-corrected FEI Titan Ultimate TEM operated at 300 kV within a single session. To obtain information about the structure of the specimen, high-angle annular dark-field (HAADF) scanning transmission electron microscopy (STEM) was performed. To provide an estimation of the In content in the quantum wells structure such that the

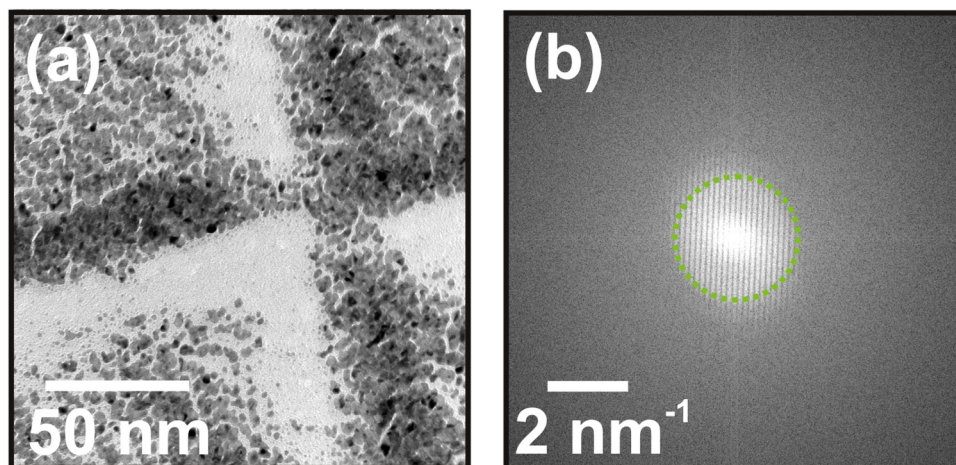


FIG. 2. (a) TEM image of a cross-grating used for aberration correction alignment after performing the correction of the Lorentz lens. (b) Fourier transform of the sum of two TEM images with a 25 nm displacement between them showing Young's fringes.

dark-field electron holography measurements could be verified, geometrical phase analysis was applied to the HAADF images.⁴⁰ To avoid artifacts, the deformation map for the growth direction was calculated from an HAADF image with the fast scan line of the STEM along the c axis of the InGaN structure and using the 0002 spot in the Fourier transform.⁴¹ The thickness of the specimen was evaluated by using convergent beam electron diffraction in two-beam conditions and was found to be 104 ± 2 nm.

For the holography experiments, first the aberrations in the Lorentz lens were corrected. Figure 2(a) shows an image of a standard cross-grating sample comprising gold particles on an amorphous carbon film acquired using the Lorentz lens. A pair of images with 25 nm displacement between them were acquired and summed. By applying a Fourier transform to the summed images, the spatial resolution in the imaging system can be evaluated from the frequency spread of the Young's fringes. Figure 2(b) shows that the information is present at 1.2 nm^{-1} corresponding to a spatial resolution of 0.8 nm, which is suitable for the holography experiments. The key when performing measurements of the electric potential by electron holography is to minimize the dynamical diffraction as this has a strong effect on the phase of the electrons.⁴² To do this, the specimen was tilted to minimize the dynamical diffraction in the bright-field image. Care was taken such that the specimen was rotated only around the [0001] growth direction axis with minimal additional tilt of the plane defined by the [1-100] and [11-20] directions. This was to avoid information about the QWs being lost in projection through the thickness of the specimen in transmission. Bright-field electron holograms with a fringe spacing of 0.8 nm were then acquired. To achieve this fine fringe spacing with a high level of contrast, the diffraction lens was adjusted to fit the electron hologram to the size of the CCD camera before focusing with the Lorentz lens.⁴³ Series of 64 electron holograms, each with an exposure time of 8 s, were acquired for both standard and pi phase shifting holography using a 4k Gatan Oneview CMOS camera. As the phase shifting holography is not dependent on the fringe spacing of the interference patterns, a relaxed fringe spacing of 2.2 nm was used to increase the contrast of the fringes and hence the sensitivity of the measurement. For the

summation of the datasets, the standard exposure comprised of 64 nominally identical holograms; the double exposure used 32 pairs of holograms shifted by π rad and the phase shifting used 16 sets of 4 holograms, each shifted by $\pi/2$ rad relative to each other and acquired for 8 s. As a consequence, it was possible to use a low beam intensity to avoid specimen damage while using a recording time of 8 min and 32 s for each holography experiment to achieve an excellent signal-to-noise ratio.

The specimen was then tilted to a two-beam diffraction condition and the (0002) diffracted beam was selected using an objective aperture. Dark-field electron holograms were then acquired using the standard and phase shifting methods. Due to the complexity of the DFEH experiments where the intensity of the dark-field interference pattern is low, the interference fringe spacing was relaxed for the standard exposure series where a fringe spacing of 1.1 nm was used to provide higher signal-to-noise deformation maps with a spatial resolution of 3.3 nm.

To help interpret the experimental results, 3D simulations of the deformation and electrostatic potentials in a TEM specimen have been performed using the NextNano software.⁴⁴ For the deformation measurements, these simulations allow an assessment of the relaxation of the thin TEM specimen. For the measurements of the electrostatic potentials, the contributions of the mean inner potential and the piezoelectric potentials can be understood. In addition, the effects of band bending at the surface of the specimens can be accounted for such that the simulation sums the potential through the projection of the TEM specimen.

RESULTS

Figures 3(a) and 3(b) show the HAADF images of the sample revealing the wurtzite structure viewed down the [11-20] zone axis and the high quality and homogeneity of the InGaN QWs, which have an average width of 2.2 nm. As examples, bright-field electron holograms with fringe spacings of 0.8 and 2.2 nm are shown in Figs. 3(c) and 3(d), respectively. Profiles of the holograms extracted from the GaN region above the QWs are shown in Fig. 3(e) where contrasts of 18% and 32% are observed, respectively. An average of

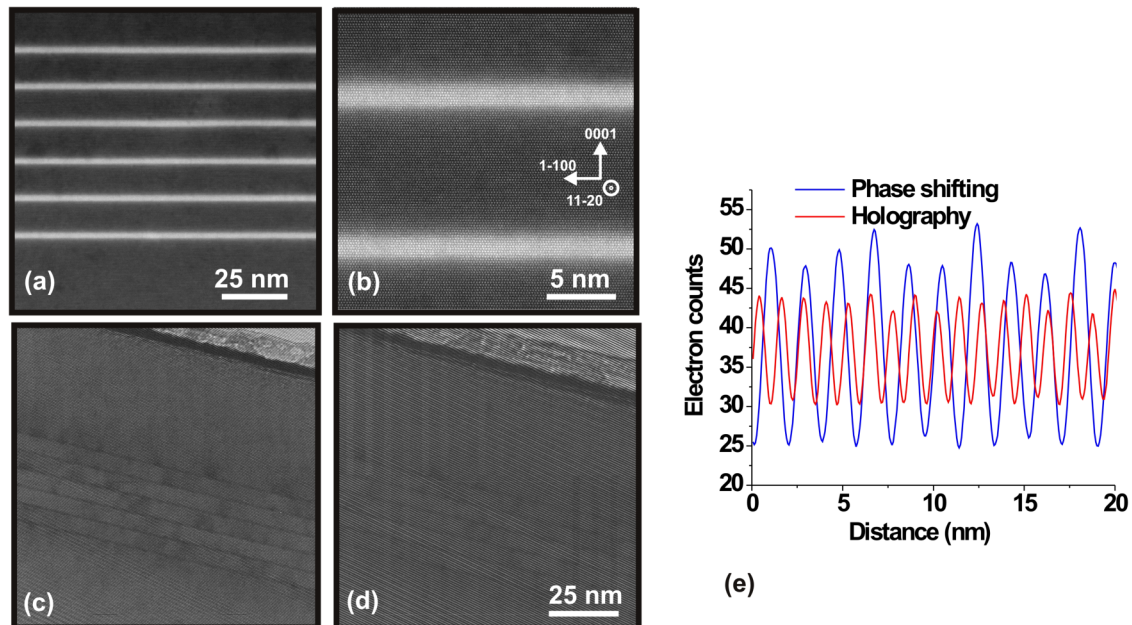


FIG. 3. (a) HAADF STEM image of the InGaN quantum wells structure. (b) Higher magnification HAADF STEM image. (c) Electron hologram of the InGaN structure acquired using standard acquisition methods and a fringe spacing of 0.8 nm. (d) Electron hologram acquired for phase shifting reconstruction with a fringe spacing of 2.2 nm. (e) Profiles showing the interference patterns acquired from the holograms in (c) and (d) from the top GaN region above the QWs.

38 electron counts are recorded in each pixel during a 8 s acquisition, which corresponds to $2 \text{ e}^- \text{ \AA}^{-2} \text{ s}^{-1}$. This is significantly lower than typical values of beam currents such as $8 \times 10^6 \text{ e}^- \text{ \AA}^{-2} \text{ s}^{-1}$ (100 pA in a 1 nm diameter probe) that have been used for approaches such as differential phase contrast (DPC) or 4D-STEM. The total electron dose for the holography experiments presented in this work is $1 \times 10^3 \text{ e}^- \text{ \AA}^{-2}$, which is significantly lower than for DPC ($1 \times 10^4 \text{ e}^- \text{ \AA}^{-2}$)⁴² and 4D-STEM ($1 \times 10^6 \text{ e}^- \text{ \AA}^{-2}$)⁴⁵ experiments that have been performed on equivalent samples.

For comparison with the bright-field holograms, Fig. 4(a) shows a detail of a dark-field hologram of the region of interest. Figure 4(b) shows the dark phase that has been reconstructed from the series of standard exposure holograms with a fringe spacing of 1.1 nm and reconstructed to provide a spatial resolution of 3.3 nm. For comparison, the bright phase from the standard exposure holography is shown in Fig. 4(c). The important experimental difference between these two phase images is that for the bright phase, the specimen is intentionally oriented to a weakly diffracting condition, and for the dark phase, the specimen is intentionally oriented to a highly diffracting two-beam condition. The phase profiles averaged across the width of the displayed images are shown in Fig. 4(d). For the dark phase, a large monotonic step in phase is observed across each QW. The change in bright phase across each QW is much lower and has a more complex form. It arises from combinations to the electrostatic potential of the mean inner potential, the piezoelectric potentials, surface charging, the possible presence of dopant atoms, and electric fields in the vacuum, which will be discussed in more detail later in the manuscript.

To obtain information about the In content in the QWs, the deformation in the growth direction, ϵ_z , was measured by performing GPA on the HAADF images as well as from standard and phase shifting electron holography. Experimental results from the GPA, phase shifting, and standard dark-field holography can be seen in Figs. 5(a)–5(c), respectively. The experimental measurements can be compared to the best fitting simulations shown in Fig. 5(d), which correspond to an In content of 20%. The profiles shown in Fig. 5(e) indicate a spread in the experimental results. As deformation measurements are obtained from the derivative of the phase, they are especially sensitive to experimental noise and artifacts. For the phase shifting dark-field holography with a spatial resolution of 0.8 nm given by the corrected Lorentz lens, ϵ_z across the layers has an average value of $3.1 \pm 0.1\%$. For the standard DFEH with a spatial resolution of 3.3 nm, ϵ_z is extremely varied across the different layers between 3.2% and 4.4% with an average value of $3.9 \pm 0.1\%$. For ϵ_z measured by GPA, a value of $3.1 \pm 0.25\%$ is obtained. The experimental measurement of ϵ_z for the GPA and the phase shifting holography are consistent with each other and from the simulations correspond to an In content of 20% in the QWs. For the standard holography, the spatial resolution of 3.3 nm is too large compared to the QWs width of 2.2 nm; thus, the deformation maps overestimate the strain by 0.9% compared to the other methods and would correspond to an In concentration of 26%.

The interpretation of the potentials is more complex due to the presence of the mean inner potential. Table I shows both simulated and experimentally measured values of the MIP that can be

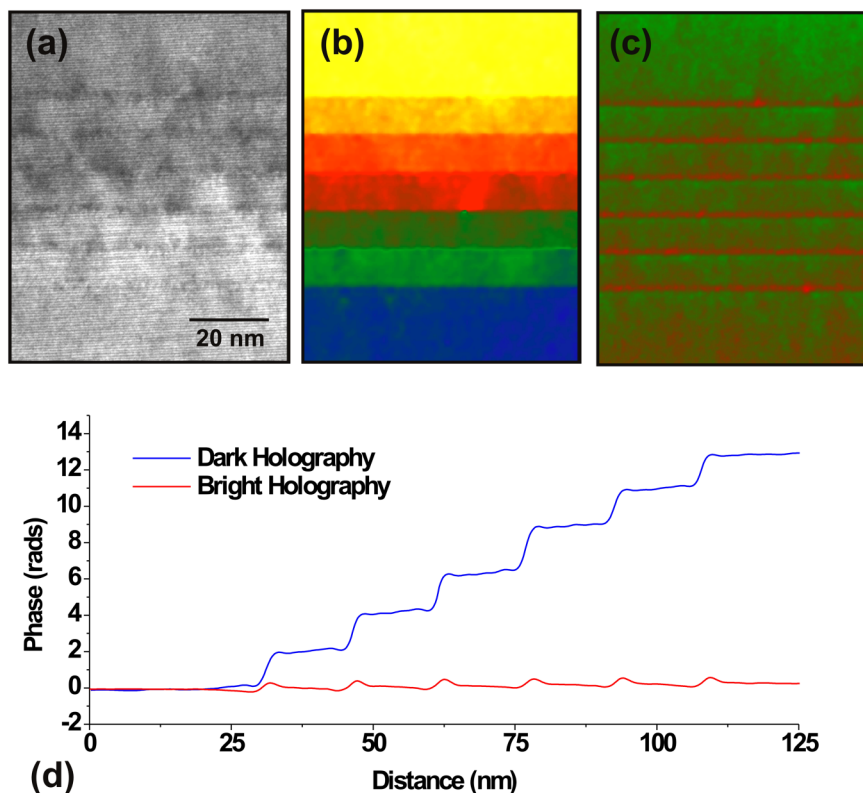


FIG. 4. (a) Example of a dark-field electron hologram. (b) Dark phase reconstructed by a standard electron holography series. (c) Bright phase reconstructed from standard holography series. (d) Phase profiles from the bright and dark phase across the regions of interest, from bottom to top of images (b) and (c).

found in the literature. From neutral atom scattering factors, V_{MIP} for GaN and InN are very similar, being 19.3 V and 19.6 V, respectively.⁴⁶ In this case, the total step in V_{MIP} between the QBs and QWs would be 0.06 V, which would still be detectable by electron

holography, but most studies of InGaN QW devices have neglected the differences in the MIP. However, the bonding must also be accounted for and density functional theory (DFT) simulations have calculated values of 16.9 V and 18.9 V for wurtzite GaN and

10 February 2025 13:43:53

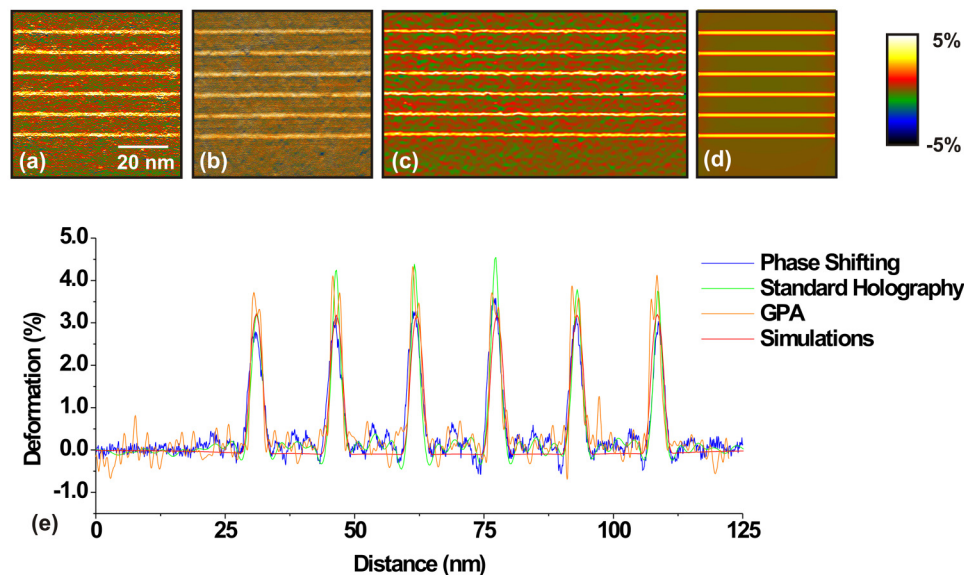


FIG. 5. ϵ_z deformation maps for the [0001] direction acquired using (a) geometric phase analysis of HAADF STEM image, (b) phase shifting holography, (c) standard holography, and (d) simulated. (e) Profiles acquired along the vertical direction of each map and averaged across 50 nm.

TABLE I. Values of V_{MIP} for GaN and InN found in the literature.

	GaN (V)	InN (V)
Neutral atom	19.3 ⁴⁷	19.6 ⁴⁷
DFT sphalerite	16.82 ⁴⁷	17.35 ⁴⁷
DFT wurtzite	16.7 ⁴⁸	18.8 ⁴⁸
Experimental	16.6 ± 0.3 ⁴⁹	...

InN, respectively.^{47,48} These simulations are confirmed by experimental measurements of V_{MIP} in GaN nanowires that have reported a value of 16.7 V.⁴⁹ Assuming a linear relationship, for a 20% In content, V_{MIP} is expected to make a 0.4 V step in potential across the QWs and QBs. In addition to the V_{MIP} contribution, the specimens also contain a symmetrical p - n junction with a nominally ionized dopant concentration of $1 \times 10^{18} \text{ cm}^{-3}$, as well as being intrinsically n -doped.⁵⁰ However, for a 100 nm thick specimen, all of the dopants are expected to be depleted through the thickness of the specimen due to the specimen surfaces; thus, no V_{dopant} contribution is expected.⁵¹ For the FIB prepared specimens, the damaged amorphous surface layers are iso-potentials, and as such, fringing fields in the vacuum around the specimen are suppressed.⁴³ For the simulations, the surfaces of the sample were pinned midgap. Figure 6 shows simulations of the potentials in 104 nm thick specimen expected for 2.5 nm thick $\text{In}_{0.2}\text{Ga}_{0.8}\text{N}$ QWs

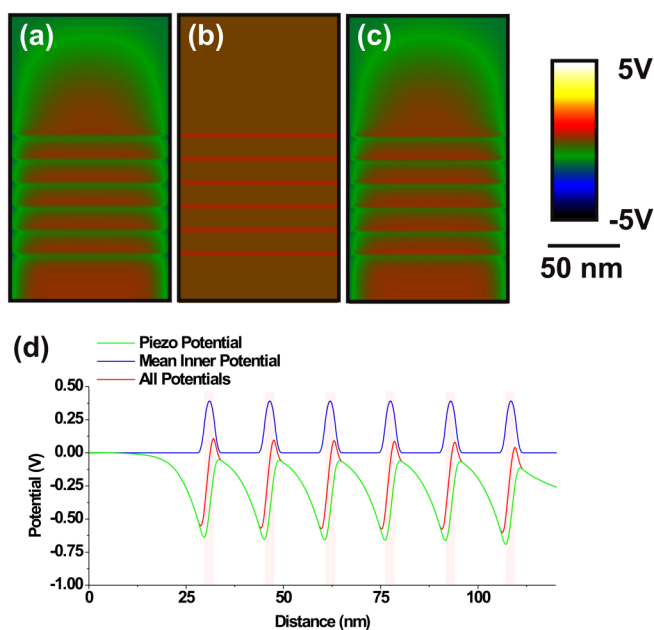


FIG. 6. Simulations of the (a) piezo potential, (b) MIP, and (c) total potential in a 104 nm thick TEM specimen with the surfaces pinned midgap. (d) Profiles of the potentials, averaged across the thickness of the TEM specimen, showing the influence of each component. The position of the QWs is indicated by the red lines.

in GaN where (a) shows the V_{piezo} component, (b) the V_{MIP} component, and (c) the combined potentials. To account for the spatial resolution of the holography, these simulations have been convolved with a Gaussian blurring of 1.2 nm. The profiles averaged from across the specimen are shown in Fig. 6(d) and reveal the large effect of the V_{MIP} on the total measured potential. From the profiles, it can be seen that in order to accurately measure V_{piezo} , it is necessary to remove V_{MIP} as it has an effect of shifting the lower value from -0.6 V to -0.5 V as indicated on the graph.

Figures 7(a)–7(c) show the maps of the electrostatic potential that have been extracted from the standard, pi phase shifting, and phase shifting holography series, respectively. These can be compared to the simulations of the electrostatic potential shown in Fig. 6. Profiles averaged across the whole width of the potential maps have been extracted and are compared to the simulations in Fig. 7(d). The total peak to peak ($V_{\text{total}} = V_{\text{MIP}} + V_{\text{piezo}}$) values of potential are less than the expected value of 0.65 V, which has been obtained from the simulations. From visual inspection of the potential maps, the phase shifting holography seems to have the lowest spatial resolution. This can be also observed as it provided the lowest measured value of the total potential. This is likely to be due to the drift of the specimen during the acquisition. For the standard holography, each individual acquisition is aligned and summed. For the phase shifting holography, a minimum of four holograms are required for each phase reconstruction, and as such, the specimen is likely to drift further during this 32 s acquisition period. In addition, for the phase shifting, some artifacts from the Fresnel diffraction at the edges of the biprism can be seen in the reconstruction,³⁵ which arises from the use of a hologram that is too narrow for the analyzed

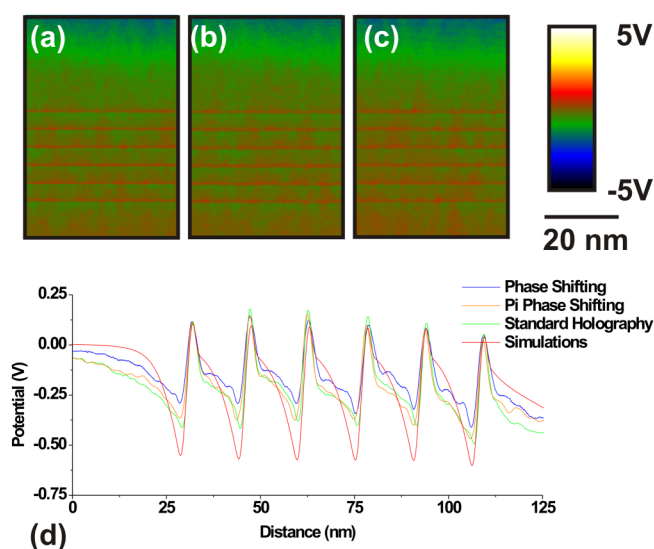


FIG. 7. Maps of the electrostatic potential for (a) standard, (b) pi phase shifting, and (c) phase shifting obtained experimentally. (d) Profiles extracted vertically for each potential map and averaged across 50 nm. The simulated total potential including the surface effects and integrated through the 104 nm thick specimen is shown.

10 February 2025 13:43:53

region of interest. For these measurements, the standard and pi phase shifting holography have recorded experimental results that appear to have the best spatial resolution, indicating that it is the tilt of the specimen and the mechanical instabilities of the specimen stage that limit the spatial resolution as much as the holography reconstruction technique.

As seen in Fig. 6(d), it is not possible to measure V_{piezo} directly from experimental potential maps due to the contribution of V_{MIP} . However, in these experiments, the high spatial resolution and sensitivity now allow the different components of the potential to be identified across the QWs. For example, Fig. 8(a) shows V_{total} measured across the QWs obtained by pi phase shifting holography. The expected V_{MIP} across the $\text{In}_{0.2}\text{Ga}_{0.8}\text{N}$ QW has been modeled and smoothed by 1.2 nm spatial resolution to correspond to the experimental measurement. The simulated V_{MIP} has then been subtracted from the experimentally measured V_{total} to give an experimental value of V_{piezo} . The criterion for the correct value of V_{MIP} is to remove the MIP bump from the potential profile and flatten it such that V_{piezo} has a similar shape as expected from the simulations of Fig. 6(d). It is not a straightforward task to accurately measure V_{MIP} and experimental measurements have a wide range in values as they are sensitive to dynamical diffraction and surface charge.⁵² Here, a value of 0.38 V has been used for the difference in V_{MIP} in Fig. 8(a), which would correspond to an In concentration of 19% in the QWs and is consistent with the values

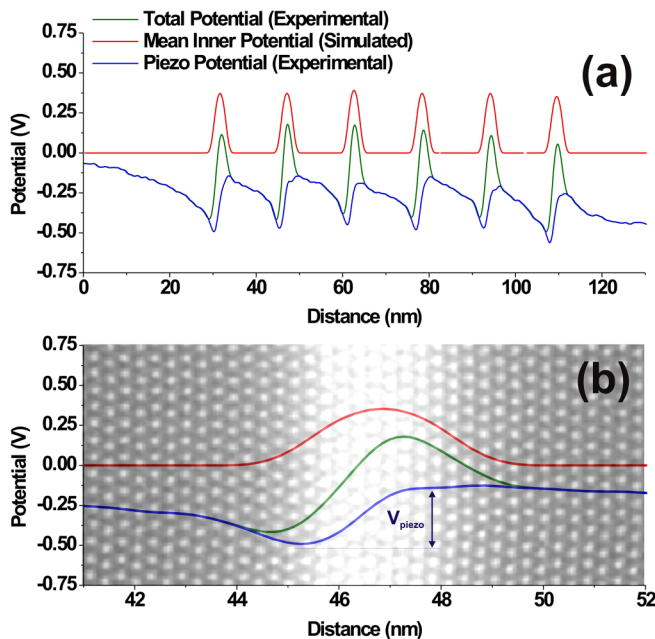


FIG. 8. (a) Experimental measurements of V_{total} across the QWs obtained using pi phase shifting holography. The simulated MIP for an In content of 19% is shown using values of V_{MIP} obtained from DFT.⁴⁸ The experimental values of V_{piezo} are obtained by subtracting the simulated V_{MIP} (b) shows a detail of the second QW indicating where the experimental measurements of V_{piezo} are obtained.

obtained from the deformation measurements.⁴⁸ Interestingly, this consistency with the strain mapping suggests that it may be possible to determine the In content directly from bright-field holography measurements of the V_{MIP} , and as such, the strain measurements are not necessary. Figure 8(b) shows a zoomed image from (a), in the region of the second QW. The individual values of the steps of V_{piezo} across each QW are shown in Table II, and an average value of 0.29 V has been obtained. The simulations provide a step of V_{piezo} of 0.6 V across 2.5 nm wide QWs. For a QW width measured experimentally of 2.2 nm, V_{piezo} of 0.53 V would be expected, which is much higher than the experimentally determined values. There are several reasons for the low measurement of V_{piezo} , the most likely is that unlike for the simulations, the QW/QB interfaces are not abrupt, plus the presence of screening of the fields due to free carriers in the specimen.³ Other reasons could be inactive thickness, which is well known for dopant mapping where positive charging of the specimen surfaces and physical damage from FIB preparation affect the potentials in the bulk of the specimen.^{53,54} We have accounted for charging of the surfaces of the specimen in the simulations by pinning the surfaces midgap, which has a small effect on the projected potentials as measured by electron holography. Due to the low electron beam dose, it is unlikely that these discrepancies are due to beam damage of the QWs, which is known to lead to the formation of In clusters.^{55,56}

To finish the analysis, it is possible to measure the electric field, E_z , across the QWs where $E(\mathbf{r}) = -\nabla V(\mathbf{r})$. The usual approach of obtaining the electric field is to apply a derivative to the experimentally measured potential. Figures 9(a)–9(d) show maps of the electric field for the standard, phase shifting, and pi phase shifting holography and simulations, respectively. The simulations of the electric field do not include any contribution from the MIP and derives only from the piezoelectric polarization. The profiles that are shown in Fig. 9(e) have been averaged across the full width of the field maps. Surprisingly, the measured values of E_z are consistent with the simulations, even though the measured values of V_{piezo} are only half than what is expected compared to the simulations. However, as can be seen in the simulations of the potentials in Fig. 6(d), for the case of these $\text{In}_{0.2}\text{Ga}_{0.8}\text{N}$ QWs, the contribution of V_{MIP} is important, and as such, these direct measurements of the E_z from the gradient of the electrostatic potential are incorrect. An alternative method that can be used is to measure the step in potential across the experimental V_{piezo} profiles that are shown in Fig. 8 and divide it by the width of the quantum well, as the electric field is assumed constant in a QW. The individual values of E_z

TABLE II. Values of the properties of each QW measured by pi phase shifting holography compared to simulations. Note that the QW width used in the simulations is 2.5 nm.

	QW1	QW2	QW3	QW4	QW5	QW6	Simulations
Width (nm)	2.2	2.4	2.2	2.2	2.1	2.1	2.5
ϵ_z (%)	2.7	3.0	3.2	3.2	3.0	3.0	3.0
V_{piezo} (V)	0.33	0.30	0.27	0.33	0.25	0.27	0.60
E_z (MV cm^{-1})	1.5	1.25	1.23	1.50	1.19	1.28	2.4

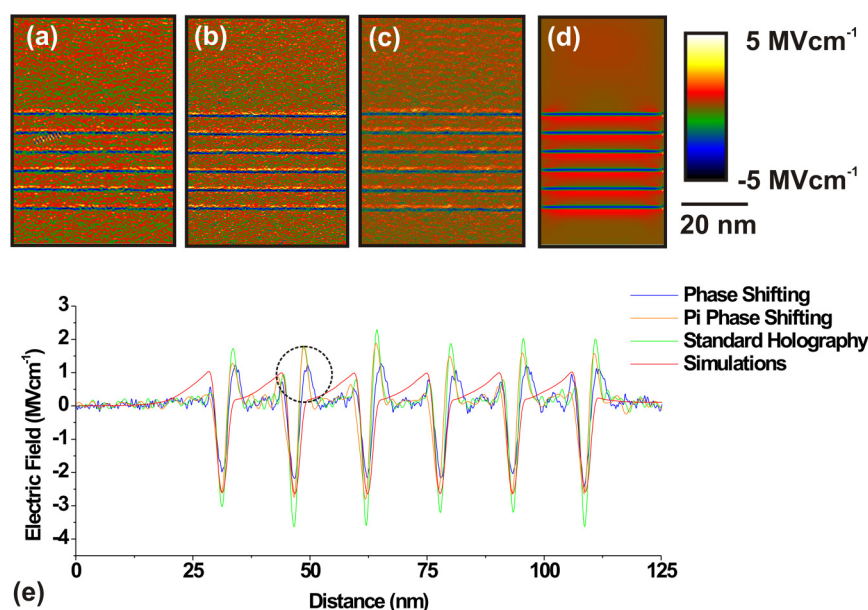


FIG. 9. Experimental measurements of E_z for (a) standard, (b) pi phase shifting, and (c) phase shifting holography. (d) Simulations of E_z that do not account for the presence of the MIP. (e) Profiles extracted vertically and averaged across 50 nm for the experimental data. Artifacts from the MIP at the top QW/QB interfaces are indicated by the dashed circle. The effect of the bottom QW/QB interfaces is not visible as they are mixed with the information about the piezoelectric field.

using this approach are shown in Table II. An average value of 1.3 MV cm^{-1} has been obtained, which are approximately half the simulated maximum value of E_z of 2.4 MV cm^{-1} .

DISCUSSION

In this manuscript, we have applied state-of-the-art electron holography to a series of InGaN QWs in GaN. The improved spatial resolution allows V_{MIP} and V_{piezo} to be separated. In most previous measurements of the potentials in wurtzite InGaN QWs, the contribution of the V_{MIP} component has been neglected. We have demonstrated that in InGaN QWs, the V_{MIP} is large compared to the V_{piezo} . As the In concentration is directly proportional to V_{piezo} , we expect V_{MIP} to strongly influence the total measured potentials for all In contents.

Although we have demonstrated that a range of holography approaches can be used to improve the spatial resolution, these measurements are still limited by instabilities, primarily specimen drift. This can be observed in the phase shifting holography results, which provided the worst spatial resolution for the measurements of the potentials, due to the incapacity to correct the specimen drift within each set of four holograms. In addition, the potential mapping was performed at the beginning of the experiment while the specimen was less stable. For the standard holography, the relatively short acquisition time of 8 s allowed the drift to be corrected within the expected spatial resolution, whereas the 32 s acquisition time for each phase shifting dataset was more sensitive to these instabilities. While this is an unsatisfying result, it is an experimental fact for many types of TEMs where the specimen stage can act in unpredictable ways. For the measurements of the potentials, spatial resolutions of 2.4 nm and 1.2 nm were obtained for the standard and pi phase shifting methods, respectively. In Fig. 7(d), it can be seen that despite these differences in spatial resolution, very

similar peak to peak results were obtained for the measurements of potential. However, when the derivative is performed such as for measurements of the deformation, the differences in spatial resolution have more influence. In terms of other factors that affect the spatial resolution, for the bright phase measurements, the specimen was tilted such that the dynamical diffraction was minimized and no information was lost in projection. However, for thicker or less perfect specimens containing defects and dislocations, this would become more complex to achieve.

For the deformation maps, the GPA and phase shifting dark-field holography, which both have spatial resolutions of less than 1 nm, give measurements of the deformation of $3.0 \pm 0.25\%$ and $3.1 \pm 0.1\%$, respectively, which suggests an In content of 20% in the QWs. For the deformation measurements by standard holography, a value $3.8 \pm 0.1\%$ has been measured with a spatial resolution of 3.3 nm. These experimental results suggest that the standard dark-field holography has provided an incorrect result, mainly due to the too lower spatial resolution. To obtain the deformation maps, it is required to calculate the derivative of the phase, which is strongly sensitive to experimental noise, as well as spatial resolution and V_{MIP} in small objects such as QWs. It is worth noting that the step in dark phase across the QWs is seven times higher than the bright phase, which should reduce the artifacts from the V_{MIP} for strain measurement; additionally, it only has an influence at the interfaces. In addition, the derivation of the monotonic dark phase is less influenced by the limitation of spatial resolution, compared to the more complex phase distributions observed in the bright phase. Importantly, the use of the GPA supports the conclusions made from the phase shifting dark-field holography measurement as it is performed on a zone axis and is not sensitive to the MIP. An important detail about the dark-field holography measurements is that the specimen is tilted to a two-beam diffracting condition, which corresponds to a rotation of 0.25° around the $[1-100]$ axis,

10 February 2025 13:43:53

leading to a loss of spatial resolution for the growth direction of 0.5 nm in projection.

Interestingly, V_{MIP} determined from the bright phase in Figs. 8(a) and 8(b) is consistent with the deformation measurements. This suggests that the DFT calculations, which until now provide the only evidence of the large differences in MIP between wurtzite GaN and InN, are correct. It also suggests that the MIP could be used to determine the In content in the QWs instead of using deformation measurements.⁵⁷ For this to be performed more routinely, more sophisticated methods for fitting and subtracting a model of V_{MIP} directly from the phase are required, such as the inclusion of interface roughness and variations of In content in the different layers. The measurement of the step in V_{piezo} across the QW is 0.29 ± 0.1 V in this work, which is half of the value expected from simulations.

In order to determine the accuracy of these measurements, a systematic study of artifacts such as the presence of an inactive thickness is required. For measuring the electric field, again the contribution of the MIP leads to incorrect calculations when the derivation of the potential profiles is used. However, values of 1.35 ± 0.15 MV cm⁻¹ have been obtained directly from the step in phase across the QW structures, which is approximately half of what is expected from our simulations.

There are alternative methods of measuring the potentials and fields in InGaN QWs by TEM with high spatial resolution. In-line holography has been used previously, in which although having high spatial resolution, V_{MIP} and V_{piezo} were not separated in a very similar specimen.²⁵ More recently, DPC and 4D-STEM, which use the deflection of the transmitted beam to directly measure the electric field, have been demonstrated.^{42,58–60} For these measurements, although high spatial resolution is possible, it has not yet been demonstrated that it is straightforward to obtain accurate measurements of the piezoelectric field in such small QW structures and whether it is possible to accurately remove the effects of the MIP, which would only appear at the QW/QB interfaces. This approach also uses a convergent beam, and as such, it would be more complicated to remove the effects from dynamical diffraction,⁶¹ although the use of precession may be able to solve these problems.⁴⁵

CONCLUSION

Off-axis electron holography can be used to measure the piezoelectric potentials in 2.2 nm wide In_{0.2}Ga_{0.8}N QWs with GaN QBs. State-of-the-art experiments combining advanced reconstruction methods, corrected Lorentz mode, automated acquisition, and hologram averaging shows high spatial resolution combined with high sensitivity. It then becomes possible to separate the contribution of the mean inner potential from the piezoelectric potential using prior knowledge of the theoretical MIP of In_xGa_{1-x}N. The measurement of the mean inner potential also provides an experimental method to measure the In content in the QWs from bright-field electron holography. More work is required to investigate the reasons for the discrepancies between the simulated piezoelectric potentials and experimentally measured values, but the non-abrupt QWs interfaces and damage from FIB preparation alone may be the reason.

ACKNOWLEDGMENTS

David Cooper acknowledges the European Research Council for funding the starting grant Stg:306535 Holoview. This work, done on the NanoCharacterisation PlatForm (PFNC) at Minatec, was supported by the “Recherches Technologiques de Base” Program of the French Ministry of Research.

DATA AVAILABILITY

The data that support the findings of this study are available from the corresponding author upon reasonable request.

REFERENCES

- ¹S. Nakamura, T. Mukai, and M. Senoh, “Candela-class high-brightness InGaN/AlGaIn double-heterostructure blue-light-emitting diodes,” *Appl. Phys. Lett.* **64**, 1687 (1994).
- ²S. Pimpitkar, J. S. Speck, S. P. DenBaars, and S. Nakamura, “Prospects for LED lighting,” *Nat. Photonics* **3**, 180 (2009).
- ³F. Della Sala, A. Di Carlo, P. Lugli, F. Bernardini, V. Fiorentini, R. Scholz, and J. M. Jancu, “Free-carrier screening of polarization fields in wurtzite GaN/InGaIn laser structures,” *Appl. Phys. Lett.* **74**, 2002 (1999).
- ⁴F. Bernardini and V. Fiorentini, “Spontaneous versus piezoelectric polarization in II-V nitrides: Conceptual aspects and practical consequences,” *Phys. Status Solidi B* **216**, 391 (1999).
- ⁵J. P. Liu, J. H. Ryou, R. D. Dupuis, J. Han, G. D. Shen, and H. B. Wang, “Barrier effect on hole transport and carrier distribution in In GaN/GaN multiple quantum well visible light-emitting diodes,” *Appl. Phys. Lett.* **93**, 021102 (2008).
- ⁶J. Zhang and N. Tansu, “Improvement in spontaneous emission rates for InGaIn quantum wells on ternary InGaIn substrate for light-emitting diodes,” *J. Appl. Phys.* **110**, 113110 (2011).
- ⁷A. Even, G. Laval, O. Ledoux, P. Ferret, D. Sotta, E. Guiot, I. C. Robin, F. Lévy, and A. Dussaigne, “Enhanced incorporation in full InGaIn heterostructure grown on relaxed InGaIn pseudo-substrate,” *Appl. Phys. Lett.* **110**, 262103 (2017).
- ⁸A. Dussaigne, F. Barbier, A. Even, B. Samuel, R. Templier, F. Lévy, O. Ledoux, M. Rozhavskaja, and D. Sotta, “Strongly reduced V pit density on InGaInOS substrate by using InGaIn/GaN superlattice,” *J. Cryst. Growth* **533**, 125481 (2020).
- ⁹R. Koester, J. S. Hwang, D. Salomon, X. Chen, C. Bougerol, J.-P. Barnes, D. L. S. Dang, L. Rigutti, A. de Luna Bugallo, G. Jacopin, and M. Tchernycheva, “M-plane core-shell InGaIn/GaN multiple-quantum-wells on GaN wires for electroluminescent devices,” *Nano Lett.* **11**, 4839 (2011).
- ¹⁰A. Tonomura, “Applications of electron holography,” *Rev. Mod. Phys.* **59**, 639 (1987).
- ¹¹W. D. Rau, P. Schwander, F. H. Baumann, W. Höppner, and A. Ourmazd, “Mapping of the electrostatic potential in transistors by electron holography,” *Phys. Rev. Lett.* **82**, 2614 (1999).
- ¹²M. R. McCartney and D. J. Smith, “Electron holography: Phase imaging with nanometer resolution,” *Annu. Rev. Mater. Res.* **37**, 729 (2007).
- ¹³H. Lichte, P. Formanek, A. Lenk, M. Linck, C. Matzeck, M. Lehmann, and P. Simon, “Electron holography: Applications to materials questions,” *Annu. Rev. Mater. Res.* **37**, 539 (2007).
- ¹⁴J. B. Park, T. Niermann, D. Berger, A. Knauer, I. Koslow, M. Weyers, M. Kneissl, and M. Lehmann, “Impact of electron irradiation on electron holographic potentiometry,” *Appl. Phys. Lett.* **105**, 094102 (2014).
- ¹⁵S. M. P. Neugebauer, H. Hoffmann, J. Witte, A. Bläsing, A. Dadgar, T. Strittmatter, T. Niermann, M. Narodovitch, and M. Lehmann, “All metalorganic chemical vapor phase epitaxy of p/n-GaN tunnel junction for blue light emitting diode applications,” *Appl. Phys. Lett.* **110**, 102104 (2017).
- ¹⁶L. Amichi, I. Mouton, V. Boureau, E. Di Russo, P. Vennéguès, P. De Mierry, A. Grenier, P.-H. Jouneau, C. Bougerol, and D. Cooper, “Correlative investigation

of Mg doping in GaN layers grown at different temperatures by atom probe tomography and off-axis electron holography," *Nanotechnology* **31**, 045702 (2019).

¹⁷L. Amichi, I. Mouton, E. Di Russo, V. Boureau, F. Barbier, A. Dussaigne, and C. Bougerol, "Three-dimensional measurement of Mg dopant distribution and electrical activity in GaN by correlative atom probe tomography and off-axis electron holography," *J. Appl. Phys.* **127**, 065702 (2020).

¹⁸F. A. Ponce, "Electrostatic energy profiles at nanometer-scale in group III nitride semiconductors using electron holography," *Ann. Phys.* **523**, 75 (2011).

¹⁹J. S. Barnard and D. Cherns, "Direct observation of piezoelectric fields in GaN/InGaN/GaN strained quantum wells," *J. Electron. Microsc.* **49**, 281 (2000).

²⁰D. Cherns, J. Barnard, and F. A. Ponce, "Measurement of the piezoelectric field across strained InGaN/GaN layers by electron holography," *Solid State Commun.* **111**, 281 (1999).

²¹M. Takeguchi, M. R. McCartney, and D. J. Smith, "Mapping In concentration, strain, and internal electric field in InGaN/GaN quantum well structures," *Appl. Phys. Lett.* **84**, 2103 (2004).

²²L. Zhou, D. A. Cullen, D. J. Smith, M. R. McCartney, A. Mouti, M. Gonschorek, E. Feltin, J.-F. Carlin, and N. Grandjean, "Polarization field mapping of heterostructures," *Appl. Phys. Lett.* **94**, 121909 (2009).

²³M. Stevens, A. Bell, M. R. McCartney, F. A. Ponce, H. Marui, and S. Tanaka, "Effect of layer thickness on the electrostatic potential in InGaN quantum wells," *Appl. Phys. Lett.* **85**, 4651 (2004).

²⁴J. Cai and F. A. Ponce, "Study of charge distribution across interfaces in GaN/InGaN/GaN single quantum wells using electron holography," *J. Appl. Phys.* **91**, 9856 (2002).

²⁵K. Song, C. T. Koch, J. K. Lee, D. Y. Kim, J. K. Kim, A. Parvizi, W. Y. Jung, G. Park, H. J. Jeong, H. S. Kim, Y. Cao, T. Yang, L.-Q. Chen, and S. H. Oh, "Correlative high-resolution mapping of strain and charge density in a strained piezoelectric multilayer," *Adv. Mater. Interfaces* **2**, 1400281 (2015).

²⁶M. R. McCartney, F. A. Ponce, J. Cai, and D. P. Bour, "Mapping electrostatic potential across an AlGaInGaN/AlGaIn diode by electron holography," *Appl. Phys. Lett.* **76**, 3055 (2000).

²⁷C. McAleese, P. M. F. J. Costa, D. M. Graham, H. Xiu, J. S. Barnard, M. J. Kappers, P. Dawson, M. J. Godfrey, and C. J. Humphreys, "Electric fields in AlGaIn/GaN quantum well structures," *Phys. Status Solidi B* **243**, 1551 (2006).

²⁸Z. H. Wu, M. Stevens, F. A. Ponce, W. Lee, J. H. Ryou, D. Yoo, and R. D. Dupuis, "Mapping the electrostatic potential across Al Ga N/ Al N/ Ga N heterostructures using electron holography," *Appl. Phys. Lett.* **90**, 032101 (2007).

²⁹M. Hÿtch, F. Houdellier, F. Hüe, and E. Snoeck, "Nanoscale holographic interferometry for strain measurements in electronic devices," *Nature* **453**, 1086 (2008).

³⁰M. Hÿtch, F. Houdellier, F. Hüe, and E. Snoeck, "Dark-field electron holography for the measurement of geometric phase," *Ultramicroscopy* **111**, 1328 (2011).

³¹A. Harscher and H. Lichte, "Experimental study of amplitude and phase detection limits in electron holography," *Ultramicroscopy* **64**, 57 (1996).

³²R. A. McLeod, M. Bergen, and M. Malac, "Phase measurement error in summation of electron holography series," *Ultramicroscopy* **141**, 38 (2014).

³³C. Gatel, J. Dupuy, F. Houdellier, and M. Hÿtch, "Unlimited acquisition time in electron holography by automated feedback control of transmission electron microscope," *Appl. Phys. Lett.* **113**, 133102 (2018).

³⁴E. Voelkl and D. Tang, "Approaching routine $2\pi/1000$ phase resolution for off-axis type holography," *Ultramicroscopy* **110**, 447 (2010).

³⁵V. Boureau, R. McLeod, B. Mayall, and D. Cooper, "Off-axis electron holography combining summation of hologram series with double-exposure phase-shifting: Theory and application," *Ultramicroscopy* **193**, 52 (2018).

³⁶V. Boureau, B. Sklénard, R. McLeod, D. Ovchinnikov, D. Dumcenco, A. Kis, and D. Cooper, "Quantitative mapping of the charge density in a monolayer of MoS₂ at atomic resolution by off-axis electron holography," *ACS Nano* **14**, 524 (2019).

³⁷V. Volkov, M. G. Han, and Y. Zhu, "Double-resolution electron holography with simple Fourier transform of fringe-shifted holograms," *Ultramicroscopy* **134**, 175 (2013).

³⁸Q. Ru, J. Endo, T. Tanji, and A. Tonomura, "Phase-shifting electron holography by beam tilting," *Appl. Phys. Lett.* **59**, 2372 (1991).

³⁹Q. Ru, G. Lai, K. Aoyama, J. Endo, and A. Tonomura, "Principle and application of phase shifting electron holography," *Ultramicroscopy* **55**, 209 (1994).

⁴⁰M. J. Hÿtch, J.-L. Putaux, and J.-M. Pénisson, "Measurement of the displacement field of dislocations to 0.03 Å by electron microscopy," *Nature* **423**, 270 (2003).

⁴¹J. J. Peters, R. Beanland, M. Alexe, J. W. Cockburn, D. G. Revin, S. Y. Zhang, and A. M. Sanchez, "Artefacts in geometric phase analysis of compound materials," *Ultramicroscopy* **157**, 91 (2015).

⁴²B. Haas, J.-L. Rouviere, V. Boureau, R. Berthier, and D. Cooper, "Direct comparison of off-axis holography and differential phase contrast for the mapping of electric fields in semiconductors by transmission electron microscopy," *Ultramicroscopy* **198**, 58 (2019).

⁴³D. Cooper, "Off-axis electron holography for the measurement of active dopants in silicon semiconductor devices," *J. Phys. D Appl. Phys.* **49**, 474001 (2016).

⁴⁴S. Birner, T. Zibold, T. Andlauer, T. Kubis, M. Sabathil, A. Trellakis, and P. Vogl, "Nextnano: General purpose 3-D simulations," *IEEE Trans. Electron Devices* **54**, 2137 (2007).

⁴⁵L. Bruas, V. Boureau, A. P. Conlan, S. Martinie, J.-L. Rouviere, and D. Cooper, "Improved measurement of electric fields by nanobeam precession electron diffraction," *J. Appl. Phys.* **127**, 205703 (2020).

⁴⁶D. Rez, P. Rez, and I. Grant, "Dirac-Fock calculations of x-ray scattering factors and contributions to the mean inner potential for electron scattering," *Acta Crystallogr. Sect. A Found. Crystallogr.* **50**, 481 (1994).

⁴⁷P. Kruse, M. Schowalter, D. Lamoén, A. Rosenauer, and D. Gerthsen, "Determination of the mean inner potential in III-V semiconductors, Si and Ge by density functional theory and electron holography," *Ultramicroscopy* **106**, 105 (2006).

⁴⁸M. Schowalter, A. Rosenauer, D. Lamoén, P. Kruse, and D. Gerthsen, "Ab initio computation of the mean inner Coulomb potential of wurtzite-type semiconductors and gold," *Appl. Phys. Lett.* **88**, 232108 (2006).

⁴⁹A. S. W. Wong, G. W. Ho, R. E. Dunin-Borkowski, T. Kasama, R. A. Oliver, P. M. Costa, and C. J. Humphreys, "The mean inner potential of GaN measured from nanowires using off-axis electron holography," *MRS Online Proc. Libr. Archive* **892**, 0892-FF11-02.1 (2005).

⁵⁰J. Neugebauer and C. G. Van de Walle, "Native defects and impurities in GaN," *Adv. Solid State Phys.* **35**, 25 (1996).

⁵¹P. Somodi, A. Twitchett-Harrison, P. Midgley, B. Kardynal, C. Barnes, and R. Dunin-Borkowski, "Finite element simulations of electrostatic dopant potentials in thin semiconductor specimens for electron holography," *Ultramicroscopy* **134**, 160 (2013).

⁵²R. S. Pennington, C. B. Boothroyd, and R. E. Dunin-Borkowski, "Surface effects on mean inner potentials studied using density functional theory," *Ultramicroscopy* **159**, 34 (2015).

⁵³A. C. Twitchett, R. E. Dunin-Borkowski, and P. A. Midgley, "Quantitative electron holography of biased semiconductor devices," *Phys. Rev. Lett.* **88**, 238302 (2002).

⁵⁴D. Cooper, C. Alliot, R. Truche, J.-P. Barnes, J.-M. Hartmann, and F. Bertin, "Experimental off-axis electron holography of focused ion beam-prepared Si p-n junctions with different dopant concentrations," *J. Appl. Phys.* **104**, 064513 (2008).

⁵⁵T. M. Smeeton, M. J. Kappers, J. S. Barnard, M. E. Vickers, and C. J. Humphreys, "Electron-beam-induced strain within InGaIn quantum wells: False indium "cluster" detection in the transmission electron microscope," *Appl. Phys. Lett.* **83**, 5419 (2003).

⁵⁶V. B. Özdöl, C. T. Koch, and P. A. van Aken, "A non-damaging electron microscopy approach to map In distribution in InGaIn light-emitting diodes," *J. Appl. Phys.* **108**, 056103 (2010).

⁵⁷D. Cooper, V. Boureau, A. Even, F. Barbier, and A. Dussaigne, "Determination of the internal piezoelectric potentials and indium concentration in InGaIn based quantum wells grown on relaxed InGaIn pseudo-substrates by off-axis electron holography," *Nanotechnology* **31**, 475705 (2020).

⁵⁸M. Lohr, R. Schregle, M. Jetter, C. Wächter, T. Wunderer, F. Scholz, and J. Zweck, “Differential phase contrast 2.0—Opening new “fields” for an established technique,” *Ultramicroscopy* **117**, 7 (2012).

⁵⁹M. Lohr, R. Schregle, M. Jetter, C. Wächter, K. Müller-Caspary, T. Mehrrens, A. Rosenauer, I. Pietzonka, M. Strassburg, and J. Zweck, “Quantitative measurements of internal electric fields with differential phase contrast microscopy on InGaN/GaN quantum well structures,” *Phys. Status Solidi B* **253**, 140 (2016).

⁶⁰N. Shibata, S. D. Findlay, H. Sasaki, T. Matsumoto, H. Sawada, Y. Kohno, S. Otomo, R. Minato, and Y. Ikuhara, “Imaging of built-in electric field at a p-n junction by scanning transmission electron microscopy,” *Sci. Rep.* **5**, 10040 (2015).

⁶¹J.-L. Rouviere, A. Béch e, Y. Martin, T. Denneulin, and D. Cooper, “Improved strain precision with high spatial resolution using nanobeam precession electron diffraction,” *Appl. Phys. Lett.* **103**, 241913 (2013).